Low Temperature Physics/Fizika Nizkikh Temperatur, 2020, vol. 46, No. 12, pp. 1394–1406

Ab initio calculations of structural, electronic and vibrational properties of $BaTiO_3$ and $SrTiO_3$ perovskite crystals with oxygen vacancies

L. L. Rusevich, E. A. Kotomin, G. Zvejnieks, and A. I. Popov

Institute of Solid State Physics, University of Latvia, Riga LV-1063, Latvia
E-mail: leorus@inbox.lv

Received July 7, 2020, published online October 21, 2020

The first-principles (*ab initio*) computations of the structural, electronic, and phonon properties have been performed for cubic and low-temperature tetragonal phases of $BaTiO_3$ and $SrTiO_3$ perovskite crystals, both stoichiometric and non-stoichiometric (with neutral oxygen vacancies). Calculations were performed with the CRYSTAL17 computer code within the linear combination of atomic orbitals approximation, using the B1WC advanced hybrid exchange-correlation functional of the density-functional-theory (DFT) and the periodic supercell approach. Various possible spin states of the defective systems were considered by means of unrestricted (open shell) DFT calculations. It was demonstrated that oxygen reduction leads to the appearance of new local vibrational modes associated with oxygen vacancies and new first-order peaks in the Raman spectra, which could be used for defect identification. The calculated Raman spectra for different vacancy positions and spins of the system, as well as other properties of defective crystals, are compared with the relevant experimental data.

Keywords: $BaTiO_3$, $SrTiO_3$, oxygen vacancy, DFT hybrid calculations, infrared spectra, Raman spectra.

1. Introduction

ABO_3-type perovskites are technologically important materials with numerous applications, including ferro- and piezoelectricity, energy harvesting, substrates for the growth of superconductors [1–17]. Thus, $BaTiO_3$ (BTO) is a typical and widely used ferroelectric material. Although the piezoelectric properties and temperature stability of pure BTO are worse than commonly used $PbZrTiO_3$, the reasonable large piezoelectric response of BTO makes it a promising material for the novel "green" BTO-based piezoelectric compounds [5, 6]. In turn, $SrTiO_3$ (STO) is an incipient ferroelectric material, which becomes ferroelectric upon external perturbation, e. g., upon doping or in thin films on substrates. Their solid solutions $(Ba,Sr)TiO_3$ (BSTO) are predicted to reveal considerably better piezoelectric properties compared to the parent materials [18, 19].

The high-temperature phases of BTO and STO reveal the ideal cubic structure, where Ti atom sits in the center of a cube and is octahedrally coordinated to six nearest O atoms. Such structure has centrosymmetric *Pm*-3*m* space group (SG 221) symmetry and therefore cannot be piezoelectric and ferroelectric. However, the situation changes upon decreasing the temperature. In BTO, at 393 K (at ambient pressure), Ti atoms are displaced from the cube center along one of main cube axes, which leads to a structural (from cubic to tetragonal *P*4*mm*, SG 99) and paraelectric-ferroelectric phase transition, accompanied by a spontaneous polarization directed parallel to the tetragonal edge of the unit cell. With the further cooling, BTO undergoes two more inter-ferroelectric structural transitions: at 278 K to the orthorhombic phase (*Amm*2, SG 38) and at 183 K to the rhombohedral phase (*R*3*m*, SG 160). All these phase transitions in BTO are of the first-order. In contrast to BTO, STO does not show piezoelectric and ferroelectric properties over a whole temperature range. At 105 K, STO undergoes the second order structural phase transition, from the paraelectric cubic phase to another paraelectric tetragonal phase (*I*4/*mcm*, SG 140). The primitive unit cell of such tetragonal lattice consists of 10 atoms, but the crystallographic (quadruple) unit cell with lattice parameters $a = b = a_0\sqrt{2}$, $c = 2a_0$ (a_0 it the lattice constant of the cubic phase) includes 20 atoms. This tetragonal phase is characterized by an antiphase rotation of TiO_6 octahedra in the nearest unit cells around the tetragonal axis c in the plane perpendicular to this axis and by a slight stretching of the unit cell. At the same time, the nearest octahedra along the c axis rotate out-of-phase around this axis.

The vibrational properties of defect-free perovskites are well studied experimentally, by means of the Raman and

infrared (IR) spectroscopy [20–27], and also theoretically (see [28–31] and references therein). There are 15 normal lattice vibrations at the Γ-point of high-temperature cubic systems of BTO and STO (with 5 atoms per unit cell). Three of them are acoustic vibrations (mode F_{1u}) and 12 — optical vibrations, which are distributed over four optical modes ($3F_{1u} + F_{2u}$). The first-order Raman scattering is forbidden in these cubic crystals due to symmetry. Three F_{1u} modes are IR-active, F_{2u} mode is a silent mode (i. e., neither Raman- nor IR-active). One of the F_{1u} modes at the Γ-point of a cubic BTO is a soft mode, which indicates on the ferroelectric cubic-tetragonal phase transition due to ferroelectric instability (displacements of the Ti cations with respect to the oxygen octahedra). The soft mode exists also at the Γ-point of the tetragonal (SG 99) phase of BTO, which corresponds to the next phase transition from the tetragonal to the orthorhombic phase. Meanwhile, a soft mode is absent at the Γ-point of a cubic phase of STO but occurs at the *R*-point of the Brillouin zone (BZ), due to the antiferrodistortive (AFD) instability (rotations of the oxygen octahedra) which leads to the phase transition to the lower symmetry tetragonal structure (SG 140). Transverse optical (TO) phonon modes at the Γ-point, calculated in this study for cubic phases of BTO and STO, are discussed below.

The vibrational representation of TO modes at the Γ-point for the tetragonal BTO phase (SG 99) is $3A_1 + B_1 + 4E$. All A_1 and E modes are here Raman- and IR-active, whereas B_1 mode is only Raman-active. One of the E modes is a soft mode. In the low-temperature tetragonal STO phase (SG 140) the Raman- and IR-active modes are strictly separated. There exist 8 IR-active, 7 Raman-active and a few silent TO modes in this phase [25]. Our calculations for vibrational frequencies of tetragonal BTO and STO are presented below.

The Raman scattering, along with thermal neutron scattering and IR spectroscopy, is widely used for investigation of lattice dynamics of bulk single crystals and ceramics [26, 27]. In particular, the Raman scattering can detect low concentrations of impurity, as well as may be used to estimate stress in materials, since the phonon frequencies are strongly sensitive to the stress. In general, structural changes that alter the crystal symmetry have a significant effect on the Raman spectrum.

One of the main point defects in perovskites is oxygen vacancies [32–37]. Oxygen vacancies with one or two trapped electrons are well known in wide-gap ionic oxides (e. g., MgO, Al_2O_3) as the F^+ and F color centers which considerably affect the optical and mechanical properties of materials [38, 39]. These defects were commonly identified by means of the optical and Raman spectroscopy [38–40]. In contrast, oxygen vacancies in perovskites with a much smaller band gap (~ 3.2–3.4 eV in both BTO and STO) show no optical absorption or luminescence. Thus, their identification is a challenging task. We are familiar only with a few experimental [41] and theoretical [42] studies of the Raman-active vibrations associated with the oxygen vacancies in STO.

In this paper, we performed *ab initio* calculations of the structural, electronic, and vibrational properties, including IR intensities and Raman spectra in the several phases of stoichiometric and oxygen-deficient BTO and STO crystals. We predicted spectral features attributed to the defect-induced phonon modes, which give the possibility to identify the defect.

2. Computational details

The first-principles (*ab initio*) computations were performed within the linear combination of atomic orbitals (LCAO) approximation as implemented in CRYSTAL17 computer code [43]. Basis sets with Hay and Wadt small core effective core pseudopotential were used for Ba, Ti, and Sr atoms [44], while for oxygen atom — the all-electron basis sets [45]. In general, the computational method is similar to that in our previous papers [18, 19, 46], devoted to the simulation of BSTO and (Ba,Ca)TiO_3 (BCTO) solid solutions. However, these solid solutions were created from BTO by substitution of Ba atoms by isovalent Sr or Ca atoms. In such cases all chemical bonds are closed, the system has no unpaired electrons. In this work, we consider oxygen vacancies due to oxygen atom removal, so that two Ti nearest atoms receive one unpaired electron each. Therefore, for defect computation, we used the unrestricted (open shell) calculations combined with the periodic supercell approach, which gives the possibility to take into account various spin states of the system with oxygen vacancy.

The supercell model allows us to simulate systems with different concentrations of defects. In the present study, oxygen vacancies in BTO were created in 2×2×2 supercell, based on the tetragonal (SG 99) BTO unit cell. Meanwhile, the vacancy can sit in either BaO plane or TiO_2 plane; each supercell with a vacancy can have two spin-state projections: $S_z = 0$ (the singlet state; the spins of two unpaired electrons are oppositely directed) and $S_z = 1$ (the triplet state; the spins have the same direction). There are eight primitive BTO unit cells in such a 40-atom supercell and, hence, it contains 24 oxygen atoms. Thus, when one oxygen atom is removed with creation of a vacancy, the BTO crystal contains a ~ 4.2 % vacancy concentration. In turn, a vacancy in STO is modeled in the low-temperature tetragonal phase of STO (SG 140). We use the crystallographic cell of tetragonal STO (keyword SUPERCON in CRYSTAL program) that contains 20 atoms in general, 12 of which are the oxygen atoms. Hence, a vacancy concentration in investigated STO crystal was ~ 8.3 %.

The computations were performed with the B1WC advanced hybrid functional [47], which combines the Wu–Cohen WC-GGA exchange functional with 16 % of the Hartree–Fock (HF) exchange and the Perdew–Wang PW-GGA correlation functional. This functional was designed

to improve the calculated electronic and structural properties of ferroelectric oxides; as we have shown, it is suitable for calculations of Ti-perovskite solid solutions (BSTO, BCTO) and STO/BTO heterostructures [19, 48]. Actually, in our previous papers [19, 46], we used three advanced hybrid exchange-correlation functionals (PBE0, B1WC, and B3LYP) for perovskites calculations. We have concluded that both PBE0 and B1WC functionals exhibit good results in calculations of different properties of BTO, STO, and $CaTiO_3$ (CTO) perovskites (PBE0 is preferable, in many cases, for the description of the structural properties; the B1WC is the best choice in calculations of the electronic properties, in particular, band gap). The B1WC functional yields also the most reliable results in computations of perovskite solid solutions [19]. The correct calculation of the band gap is especially important for the investigation of oxygen vacancies and positioning the vacancy energy level in the band gap (oxygen vacancies in BTO and STO are quite "shallow" defects [35]). Therefore, we used the B1WC functional in the present work similar to Ref. 48.

We have performed a complete vibrational analysis of BTO and STO crystals (without and with oxygen vacancies), including the Raman and IR spectra computations. At the beginning, full geometry optimization was carried out and the equilibrium geometry was found. The atomic structure of the crystal was optimized by using the analytical energy gradients with respect to atomic coordinates and unit cell parameters. Convergence was checked on both gradient components and nuclear displacements.

The total static dielectric tensor ε_{ij}^{0}, which is the sum of the electronic and the vibrational components ($\varepsilon_{ij}^{0} = \varepsilon_{ij}^{\infty} + \varepsilon_{ij}^{\mathrm{vib}}$), was estimated in two steps. Firstly, the high-frequency dielectric tensor $\varepsilon_{ij}^{\infty}$ has been calculated through the coupled perturbed Hartree–Fock/Kohn–Sham (CPHF/CPKS) scheme [49], adapted for periodic systems [50]. After that, TO vibrational frequencies at the Γ-point were calculated within the harmonic approximation. The vibrational contribution $\varepsilon_{ij}^{\mathrm{vib}}$ to the total static dielectric tensor was also calculated.

The integrated intensity I_n of the IR vibrational mode ν_n is computed under the hypothesis of isotropic response (i. e., for powder sample). Three different techniques may be used in the CRYSTAL17 code for the IR intensities calculation: through the Berry phase, Wannier functions, and CPHF approach [43, 51]. The first two approaches imply numerical differentiations, while the latter is entirely analytical. We have used calculations of the IR intensities through both the Berry phase and CPHF approach. A comparison of obtained results shows that the two methods give close intensities, the difference rarely exceeds a few percent. In turn, intensities of the Raman scattering are calculated in CRYSTAL17 by a fully analytical method, which is based on the self-consistent solution of first- and second-order CPHF/CPKS equations for the electronic response to external electric fields at the equilibrium geometry [52, 53]. Finally, the Raman intensities were normalized per the most intensive line.

Besides intensity, it is possible to calculate IR and Raman spectra, using TO vibrational modes. In the present study, we summarize below the calculated IR intensities in tables and the Raman spectra in figures. The Raman spectra $A(\nu)$ are computed for both cases of polycrystalline powder sample (total intensity, parallel polarization, perpendicular polarization) and single-crystal sample (*xx*, *xy*, *xz*, *yy*, *yz*, *zz* polarizations). We use spectra of the total intensity of a powder sample in the figures. All peaks are described by the Lorentzian function:

$$A(\nu) = \sum_{n} \frac{I_n}{\pi} \frac{\gamma_n / 2}{(\nu - \nu_n)^2 + \gamma_n^2 / 4}, \qquad (1)$$

where ν_n and I_n are the computed TO frequencies and Raman intensities, respectively, for each mode *n*; γ_n is the full width at half maximum ($\gamma_n = 8$ cm^{-1} by default).

Note that the symmetry of systems strongly decreases after vacancy creation. This fact in combination with open-shell calculations leads to the essential demand of the additionally computation time. On the other hand, the study of the vibrational properties is computationally demanding due to the necessary high accuracy of the calculations. To balance the computation time and accuracy of calculations, we have set, in particular, the truncation of infinite lattice sums in the two-electron integral evaluation (tolerances for Coulomb and exchange sums) to 8, 8, 8, 8, 16; the SCF convergence threshold on total energy was set to 10^{-10} Ha; a Monkorst–Pack mesh of points in reciprocal space was used with shrinking factor 12, 8 or 6 for bulk (pure BTO and STO in cubic and tetragonal phases), crystallographic STO cell (tetragonal phase with and without vacancy) and supercell BTO (the tetragonal phase with and without vacancy) calculations, respectively. A high level of DFT integration accuracy ("extra extra large grid" XXLGRID) was kept for all calculations. The following computational parameters were used during a full geometry optimization in order to achieve a very accurate minimum on the potential energy surface required for frequency calculation: threshold for energy change between two geometry optimization steps (TOLDEE) is 10^{-10} Ha; RMS on gradient (TOLDEG) is 0.00003 Ha/Bohr; RMS on estimated displacements (TOLDEX) is 0.00012 Bohr.

In order to test the supercell approach for the IR and Raman spectra calculations, we calculated these spectra for pure (without vacancies) BTO and STO bulk crystals in tetragonal phases (SG 99 for BTO and SG 140 for STO, standard calculation with one primitive unit cell) and for supercells (similar calculations will be then performed for the crystal with defect). The results of both types of computations almost completely coincide.

3. Results and discussion

3.1. Properties of bulk BTO and STO crystals in cubic and tetragonal phases

Before performing the calculations on oxygen vacancies, we have checked how our computational scheme reproduces the structural, electronic, dielectric, and vibrational properties of pure bulk BTO and STO crystals in both cubic and tetragonal phases.

The calculated and experimental basic bulk properties of BTO and STO in a cubic phase (SG 221) are presented in Table 1, while their vibrational properties in Table 2 (BTO) and Table 3 (STO). Both BTO and STO in a cubic phase exhibit a centrosymmetric cubic structure that can be described by three symmetry-irreducible atoms in the unit cell; both crystals have the indirect band gap in this phase. As it is seen from Table 1, calculated data, including high-frequency dielectric constant, are in good agreement with existing experimental data. The vibrational contribution ε_{vib} to the total static dielectric tensor will be discussed below.

Table 1. The lattice constant a, indirect band gap E_g, high-frequency dielectric constant ε_∞ and vibrational part ε_{vib} of total dielectric constant for the cubic structures (SG 221) of BTO and STO

Parameter	BTO		STO	
	Calculation	Experiment	Calculation	Experiment
a, Å	3.975	3.996 [54]	3.884	3.905 [55]
E_g, eV	3.20	3.2 [56]	3.36	3.25 [57]
ε_∞	5.50	5.24 [58]	5.09	5.18 [58]
ε_{vib}	3.4		524.6	310 [59]

Let us discuss now vibrational properties of BTO and STO crystals in a cubic phase. In Tables 2 we report the calculated TO phonon frequencies at the Γ-point of BZ and evaluated through the Berry phase approach IR intensities for these modes in BTO crystal. Table 3 reveals the same information for STO crystal as well as experimental data for STO phonon frequencies (to the best of our knowledge, no experimental phonon frequencies have been reported for the BTO cubic phase). The vibrational features of these two crystals in a cubic phase are in many respects similar. The TO vibrational representation of BTO or STO contains four triply degenerate modes ($3F_{1u} + F_{2u}$); one more F_{1u} mode is an acoustic mode. Three TO F_{1u} modes are IR-active (there are corresponding calculated IR intensities in the tables), while F_{2u} mode is silent. Due to symmetry, the first-order Raman scattering is forbidden in *Pm*-3*m* centrosymmetric cubic systems. At the same time, IR-active modes are induced by all 5 atom displacements, but the silent mode is connected with the displacements of the O atoms only.

Table 2. Pure BTO (SG 221, bulk), calculated TO frequencies (cm^{-1}) and integrated IR intensities I_{calc} (km/mol)

Mode	Calculation	I_{calc}
F_{1u}	–207	—
F_{1u}	199	464
F_{2u}	313	—
F_{1u}	487	189

Note: F_{2u} is a silent mode. Negative frequency indicates a soft mode; IR intensity is not reported for this mode with imaginary frequency.

Table 3. Pure STO (SG 221, bulk), calculated and experimental TO frequencies (cm^{-1}) and calculated integral IR intensities I_{calc} (km/mol)

Mode	Calculation	Experiment [25]	I_{calc}
F_{1u}	69	93	8568
F_{1u}	175	176	118
F_{2u}	259	266	—
F_{1u}	559	548	1748

Note: F_{2u} is a silent mode.

Now we discuss the vibrational contribution ε_{vib} to the total static dielectric tensor (see Table 1). In STO ε_{vib} is quite large; TO_1 mode with the lowest frequency (69 cm^{-1}, see Table 3) gives the main contribution. It is expected, because the vibrational contribution ε_{vib} is inversely proportional to the second power of phonon frequency [30]. We observe even an overestimate of the calculated value with respect to the experimental one. On the contrary, in BTO the calculated vibrational contribution is small — more than two orders of magnitude less than the calculated ε_{vib} in STO. This is due to the presence of a soft mode at the Γ-point in BTO, unlike STO. In the real crystal frequency of this mode is small and positive, and it decreases down to zero with temperature decrease till the phase transition point. In the computer simulations (performed at 0 K) this soft mode reveals an imaginary frequency (Table 2). During ε_{vib} calculation, the contribution of such an imaginary mode was neglected. Actually, only low-frequency soft modes give the largest contribution to ε_{vib}, but since in our calculations such phonon frequencies are imaginary they are not taken into account. In the same way, modes with imaginary frequencies are not taken into account also in the Raman and IR spectra calculations.

The soft mode (imaginary phonon modes at the Γ-point in our calculations) in a cubic phase of BTO indicates at the structural instability in the system. It is a ferroelectric phase transition to the tetragonal phase (SG 99) connected with the displacement of Ti atoms from the centers of octahedra and destruction of the centrosymmetric structure. As this phase transition is connected with the soft mode at the Γ-point, it takes place without an increase of the number of atoms in the primitive cell [29]. Therefore, the total

number of normal lattice vibrations in the tetragonal phase remains 15, as in a cubic phase. The calculated basic bulk properties of BTO in the tetragonal phase (SG 99) are presented in Table 4 along with the available experimental data; calculated and experimental TO phonon frequencies as well as calculated IR intensities are seen in Table 5.

Let us note several moments concerning BTO properties in Table 4. Our calculations give the indirect band gap for the tetragonal phase of BTO, similar to the cubic phase. Due to symmetry reason, the dielectric tensor of BTO in a tetragonal phase contains two independent components. The elements of optical dielectric tensor ε^{∞}, obtained in our calculations, are devoid of significant overestimate, mentioned in Ref. 61, and reveal not only the correct ratio $\varepsilon^{\infty}_{xx} > \varepsilon^{\infty}_{zz}$, but also values close to experimental ones. The vibrational contribution to the static dielectric tensor is small again (as in a cubic phase); this is related to a soft mode at the Γ-point of the tetragonal phase of BTO (see Table 5), corresponding to the structural instability and the next phase transition from the tetragonal to the orthorhombic phase.

Let us consider phonon modes at the Γ-point of the BTO tetragonal phase (Table 5). In the tetragonal phase, each of the three F_{1u} modes of the cubic phase (Table 2) is split into the A_1 (nondegenerate) and E (with the degeneracy 2) modes, but a silent F_{2u} mode is split into the B_1 (nondegenerate) and E modes. Thus, the vibrational representation of TO modes at the Γ-point for the tetragonal BTO phase is $3A_1 + B_1 + 4E$. At the same time, one of the E modes is the soft mode. In the ferroelectric phase, without the center of inversion, the vibrations may be active both in the IR and in the Raman spectra. Our calculations reveal that all A_1 and E modes are both Raman- and IR-active, whereas B_1 mode is Raman-active only. It is interesting that all A_1 modes are connected with displacements of all five atoms along the z axis (tetragonal axis), all E modes are induced by displacements of all atoms in the plane xy, but B_1 mode (IR-inactive) is connected with displacements of equatorial oxygen atoms (located in the TiO_2 plane) only and only along the z axis. Table 5 reveals that calculated phonon frequencies agree well with the experimental data, maybe except for one A_1 mode (calculated 330 cm^{-1} vs. experimental 270 cm^{-1}).

Table 4. Lattice constants a and c, band gap E_g, the electronic (high frequency) ε^{∞} and vibrational ε^{vib} contributions to the total static dielectric tensor for the tetragonal structures of BTO (SG 99) and STO (SG 140)

Parameter	BTO		STO	
	Calculation	Experiment	Calculation	Experiment
a, Å	3.962	3.992 [54]	5.488	5.507[a]
c, Å	4.048	4.036 [54]	7.777	7.796[a]
E_g^b, eV	3.26	3.38 (3.27) [56]	3.39	3.43 [60]
$\varepsilon^{\infty}_{xx}$	5.28	5.19[c]	5.1	
$\varepsilon^{\infty}_{zz}$	4.81	5.05[c]	5.1	
ε^{vib}_{xx}	3.6		1131.7	
ε^{vib}_{zz}	19.2		886.8	

Note: [a]Taken from [28]. [b]For BTO calculated indirect band gap, experimental values [56] at room temperature for light polarized parallel (and perpendicular) to the ferroelectric c axis; for STO calculated direct band gap. [c]Taken from [61].

Table 5. Pure BTO (SG 99, bulk), calculated and experimental TO frequencies (cm^{-1}), and calculated integral IR intensities (km/mol)

Mode	Calculation	Experiment [62]	I_{calc}
E	–130	soft	—
A_1	186	170	230
E	193	180	303
B_1	307	305	—
E	315	305	18
A_1	330	270	1704
E	487	486	197
A_1	539	520	557

Note: All vibrational modes are Raman-active, B_1 mode is IR-inactive. Negative frequency indicates soft mode; IR intensity is not reported for this mode with imaginary frequency.

Now we return to the structural cubic-tetragonal phase transition in STO. As it is seen in Table 3, the soft mode is absent at the Γ-point of STO cubic phase; however, it exists at the R-point [28] (phonon calculations at the R-point are beyond the scope of the present study). Antiferrodistortive structural instability (static rotations of the oxygen octahedra around the tetragonal axis) in STO, which leads to the second-order phase transition to the tetragonal structure of $I4/mcm$ symmetry (SG 140), is connected with this soft mode. Note that Ti atoms are symmetry-constrained to move along the tetragonal axis in such a structure. Meanwhile, the splitting of the threefold degenerate cubic phonon modes and appearance in the tetragonal phase of IR- and Raman-active modes occurs in a much more complex way [27].

The calculated basic bulk properties of the STO in tetragonal phase (SG 140) are presented in Table 4 along with the available experimental data. We have obtained 3.2° for the angle of octahedra rotation (experimental value of 2.1° at 4.2 K [63]); the calculated band gap is changed from the indirect in the cubic phase to direct in the tetragonal phase and is very close to the experimental one.

There are 30 normal lattice vibrations (3 acoustic and 27 optical) at the Γ-point of the tetragonal STO with 10 atoms per a primitive unit cell. The calculated and experimental TO phonon frequencies at the Γ-point and evaluated through the Berry phase IR intensities for these modes are presented in Tables 6.1–6.3. Additionally, data are clas-

Table 6.1. Pure STO (SG 140, bulk), calculated and experimental IR-active TO frequencies (cm^{-1}), and calculated integral IR intensities (km/mol)

Mode	Calculation	Experiment [25]	I_{calc}
E_u	47	15	11441
A_{2u}	53		5812
E_u	173	172	217
A_{2u}	175		63
E_u	260		0.3
E_u	453.64	436	20
E_u	554	548	2222
A_{2u}	556		1107

sified into IR-active (Table 6.1), Raman-active (Table 6.2) and silent (Table 6.3) modes. Note that Raman- and IR-active modes are strictly separated in this phase. Eight modes are IR-active ($3A_{2u} + 5E_u$), seven are Raman-active ($A_{1g} + B_{1g} + 2B_{2g} + 3E_g$) and four are silent ($A_{1u} + 2A_{2g} + B_{1u}$). This analysis completely coincides with results [28]. Let us add that IR-active mode E_u with the lowest frequency (47 cm^{-1}) and the highest IR intensity gives the main contribution to ε_{xx}^{vib} component of vibrational dielectric tensor, while A_{2u} IR-active mode (53 cm^{-1}) gives the main contribution to ε_{zz}^{vib} component.

As the tetragonal phases of stoichiometric BTO and STO reveal the Raman-active modes (Tables 5 and 6.2), we calculated the relevant Raman spectra in Fig. 4 (BTO) and Fig. 5 (STO). Analysis shows that the two most intensive peaks of BTO are connected with two A_1 TO phonon modes (330 and 539 cm^{-1}). As was noted above, all A_1 modes arise due to displacements of all five atoms of the primitive cell along the tetragonal axis. The analysis of the displacements of each atom contributing to this mode reveals that in the case of a line of 330 cm^{-1} the maximal displacements show Ti atoms and equatorial oxygen atoms (which lie in TiO_2 planes), meanwhile, Ti and oxygens atoms oscillate in antiphase. In contrast, for the line of 539 cm^{-1} the axial oxygen atoms (in BaO planes) reveal

Table 6.2. Pure STO (SG 140, bulk), calculated and experimental Raman-active TO frequencies (cm^{-1})

Mode	Calculation	Experiment [21], [25]
E_g	21	15, 40
A_{1g}	75	48, 52
E_g	146	143, 144
B_{2g}	148	235, 229
B_{2g}	453.62	
E_g	454.2	460, 447
B_{1g}	497	

Table 6.3. Pure STO (SG 140, bulk), calculated silent TO frequencies (cm^{-1})

Mode	Calculation
B_{1u}	263
A_{1u}	453
A_{2g}	495
A_{2g}	872

the maximal displacements. As for the STO calculated Raman spectrum, it has four main peaks: at 75 cm^{-1} (A_{1g}), 148 cm^{-1} (B_{2g}), 453.62 cm^{-1} (B_{2g}) and 497 cm^{-1} (B_{1g}). Two latter peaks are the most intensive. Interestingly, the vibrations of Ti atoms do not take part in the STO Raman spectrum formation. With respect to the above-mentioned four main peaks in the spectrum, all of them are formed by rotating (equatorial) oxygen atoms, which oscillate in the *xy* plane. Additionally, Sr atoms vibrating along the tetragonal axis give some contribution to both B_{2g} lines, too, although, actually, this contribution for the line 453.62 cm^{-1} is negligible.

A direct comparison of calculated and experimental Raman spectra is not trivial because real sample may contain some impurities, defects, grains, stresses, etc. In addition, it is necessary to take into account growth conditions and post-growth treatments of the sample as well as experimental conditions. Our calculated spectra are the first-order Raman spectra and include TO vibrational modes only. Therefore, in this paper, we focus mainly on a comparison of the calculated Raman spectra in pure and defective systems rather than a comparison of calculated and experimental spectra. However, speaking on available experiments, Perry and Hall [20] reported the BTO Raman spectrum at 290 K, with two peaks due to TO phonon modes. These peaks at 307 and 518 cm^{-1} are quite close to the main peaks in our calculated spectrum of tetragonal BTO (330 and 539 cm^{-1}). Moreover, additional calculation of longitudinal optical (LO) phonons contributes into our Raman spectrum one more line with significant intensity at 762 cm^{-1} (this mode corresponds to LO-TO splitting for TO mode at 330 cm^{-1}). Note experimental peak at 722 cm^{-1} related to the LO mode [20], which is also not so far from our calculated frequency.

3.2. BTO and STO crystals with oxygen vacancies

3.2.1. Atomic and electronic structure

The oxygen vacancy (V_O) is a common defect in perovskites. Most simulations concerning oxygen vacancies in the Ti-containing $ATiO_3$ perovskites deal with the cubic paraelectric phase of these crystals. It may be reasonable for STO with its cubic structure at room temperature (RT), but BTO reveals the tetragonal structure at RT and the cubic phase is its high-temperature phase. In this

section, we discuss oxygen vacancies in the tetragonal phases of bulk BTO and STO, including vibrational properties and the Raman spectra of these crystals.

When simulating an oxygen vacancy, it is important to understand changes in structural and electronic properties induced by the defect, which depend mainly on the Ti–O chemical bonds [32]. Perfect BTO and STO crystals have a mixed ionic-covalent nature of the chemical bonding, which is characterized by the effective charges different from the formal charges of Ba^{2+}, Sr^{2+}, Ti^{4+}, and O^{2-} ions. Thus, our calculated Mulliken atomic charges are +1.8|*e*| on Ba, +2.31|*e*| on Ti, –1.35|*e*|…–1.38|*e*| on O atoms in tetragonal BTO and +1.87|*e*| on Sr, +2.32|*e*| on Ti, –1.39|*e*|…–1.4|*e*| on O atoms in tetragonal STO. It is seen that Ba and Sr demonstrate the most ionic bonding in crystals, while the Ti and O reveal the considerable covalence of their chemical bonds.

When forming the neutral oxygen vacancy, the neutral O atom is removed from the crystal lattice site. Its creation markedly changes the electronic states of two the nearest to the defect Ti atoms, which were connected with a removed O atom. Each of these Ti atoms receives one unpaired electron and, therefore, it is necessary to use the unrestricted (open-shell) calculations for the simulation of such a defective system. The system with such defect may have two different spin states: $S_z = 0$, when two unpaired electrons are oppositely directed, and $S_z = 1$, when both spins have the same direction. We performed calculations for both specified spin states. In our calculations, we did not strive to reach the limit of well-separated vacancies and completely eliminate the interaction of periodically repeated defects, as it was done in [36], for example. Large supercells are required for this aim (270–320-atom supercell [36]), but open-shell calculations are very demanding on computing resources. We performed our calculations for $BaTiO_{3-\delta}$ with $\delta = 0.125$, what correspond to 4.17 % of vacancy concentration (relatively of the number of O atoms in the system); for the $SrTiO_{3-\delta}$ structure $\delta = 0.25$, corresponding to 8.33 % of defect concentration. These concentrations correspond to the volume vacancy density of $1.9 \cdot 10^{21}$ and $4.1 \cdot 10^{21}$ cm^{-3} for BTO and STO, respectively. It is necessary to say that, in general, these are considerable defect concentrations [41]. The minimal distance between periodically repeated vacancies in these structures is about 8 and 5.5 Å for BTO and STO, respectively.

In general, the oxygen vacancy can be located in either the TiO_2 plane or (Ba/Sr)O plane (the planes are perpendicular to the tetragonal *c* axis). Both these cases are shown in Fig. 1 to Fig. 3 for the BTO supercell. Perfect tetragonal BTO structure is presented in Fig. 1, where two oxygen atoms are marked, to be removed with the creation of vacancy in either TiO_2 or BaO planes. In the Figs. 2 and 3, BTO structures are presented with oxygen vacancy in the planes TiO_2 (between atoms Ti2 and Ti4) and BaO (between atoms Ti1 and Ti2), respectively. These figures demonstrate the local lattice relaxation around the defects

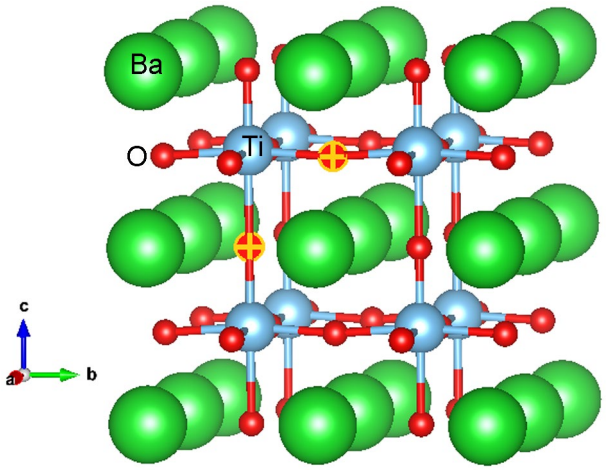

Fig. 1. BTO without vacancy (SG 99). The marked oxygen atoms will be removed for creations of vacancies in the TiO_2 (see Fig. 2) and BaO (Fig. 3) planes.

with $S_z = 0$. For example, when the equatorial oxygen atom was removed (in TiO_2 plane, Fig. 2), the distance between the nearest to the vacancy Ti atoms (Ti2 and Ti4) increases from 3.96 Å in a perfect crystal to 4.34 Å in a defective crystal (9.6 %); whereas after removing the axial oxygen atoms (BaO plane, Fig. 3), the distance between the nearest to the vacancy Ti atoms (Ti1 and Ti2) changes from 4.05 to 4.40 Å (8.6 %).

The calculated basic properties of perfect (tetragonal) and defective (systems with different spin states and oxygen vacancy in different planes) BTO and STO supercells are summarized in Tables 7 and 8, respectively. The lattice parameters in the tables represent the length of the edges of the supercell (*a*, *b*, *c*), the angles between the edges (α is the angle between *b* and *c* edges, β = *a*^*c*, γ = *a*^*b*), and the

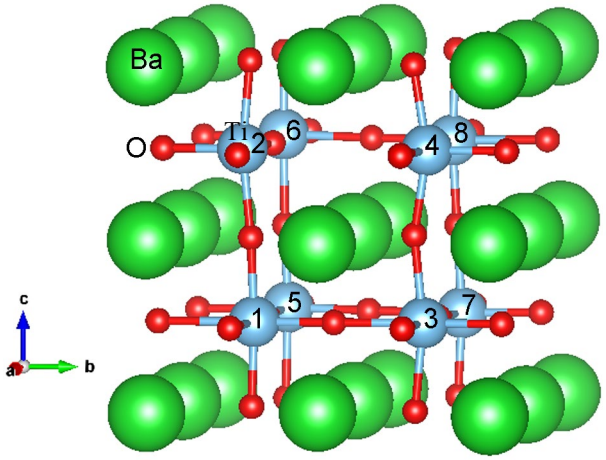

Fig. 2. BTO with the vacancy in plane TiO_2 (the equatorial oxygen atom between atoms Ti2 and Ti4 was removed). The spin state of system $S_z = 0$, SG 1. All Ti atoms in supercell are numbered.

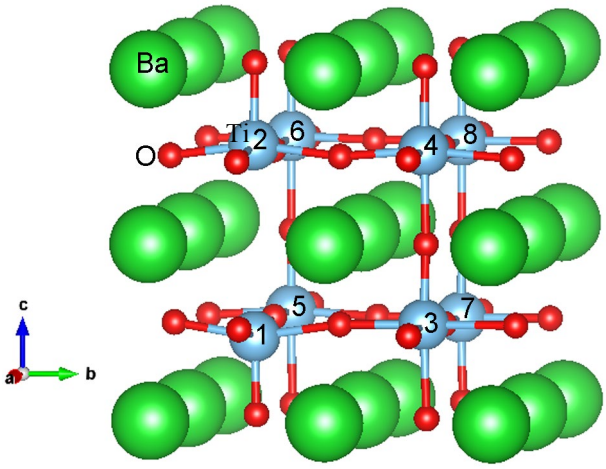

Fig. 3. BTO with the vacancy in plane BaO (the axial oxygen atom between atoms Ti1 and Ti2 was removed). The spin state of system $S_z = 0$, SG 8. All Ti atoms in supercell are numbered.

volume of supercell V. Additionally, we presented the band gap for perfect crystals or the defect ionization energy (the distance between the bottom of the conduction band and the energy band corresponding to the vacancy) for defective system E_g^i and the vacancy formation energy E_{vac}.

Let us note some common results concerning vacancy calculations in BTO and STO. First, defective and perfect crystals have substantially different symmetry. For the BTO structures (see Table 7) with a vacancy in the BaO plane, space group symmetry corresponds to SG 8, but for a vacancy in the TiO_2 plane any symmetry is lost, SG 1. For STO structures with defect (Table 8) symmetry corresponds to SG 6. As it is seen from Tables 7 and 8, the volume of supercells increases upon the creation of vacancies. Meanwhile, distortions of the crystallographic angles are quite small: the deviation from 90° for BTO does not exceed 0.3°, but for STO (with 2 times higher concentration of defects) — 1.6°. Thus, in general, there is no essential changes in the average crystal structures, which confirms we use acceptable defect concentrations.

To estimate the formation energy of oxygen vacancy in the crystals, the following expression was used [36]:

$$E_{vac} = E(V_O) + E(O) - E(\text{perfect}), \qquad (2)$$

where $E(V_O)$ and E(perfect) are the total energies of the defective and perfect crystals, respectively, and E(O) is a half of the energy of a gas-phase O_2 molecule in the triplet state. The equilibrium bond length (1.23 Å) and the binding energy (5.4 eV) of O_2, calculated in the present study, are in good agreement with the reported in Ref. 64 calculated and experimental data. Authors [36] noted that *ab initio* calculations of formation energy for oxygen vacancies in bulk STO give results within the range of 6.8–8.5 eV. Our results are in the same range, too, and only slightly differ for BTO and STO crystals.

Tables 7 and 8 demonstrate that the structural properties, as well as defect formation energy, weakly depend on the spin state of a crystal. As a further confirmation of this statement let us return to the mentioned above local lattice distortions around the defect, e. g., the variation of the distances between the nearest to the vacancy Ti atoms. They move away from the vacancy due to mutual repulsion. Thus for the vacancy in the BaO plane (Fig. 3) the distance between atoms Ti1 and Ti2 increases from 4.050 Å (perfect crystal) to 4.400 Å ($S_z = 0$) and 4.405 Å ($S_z = 1$). For the vacancy in the TiO_2 plane the corresponding distance changes from 3.880 Å (perfect crystal) to 4.297 Å ($S_z = 0$) and 4.295 Å ($S_z = 1$). The latter total displacements of Ti atoms outwards oxygen vacancy (~ 0.4 Å) very well agree with results obtained in Ref. 65 for the vacancy in tetragonal STO. It should be also noted that the triplet state (with $S_z = 1$) is energetically slightly more favorable than the singlet state ($S_z = 0$) for both BTO and STO, in agreement with conclusions [64]. We show below that vibrational (as opposed to structural) properties of the defective solids depend significantly on the spin state of the system. Before this, however, we briefly discuss the electronic properties of systems with oxygen vacancies.

There are two important points concerning the electronic properties of defective systems. First, the conductivity

Table 7. Vacancy in BTO. Calculations with supercell 2×2×2 (40 atoms)

Parameter	Perfect BTO SG 99	BTO with vacancy (4.17 %)		
		in BaO, $S_z = 0$	in BaO, $S_z = 1$	in TiO_2, $S_z = 0$
a, Å	7.925	7.969	7.975	7.968
b, Å	7.925	7.969	7.975	8.078
c, Å	8.096	8.075	8.070	7.966
α, deg	90	89.995	89.972	90.002
β, deg	90	89.995	89.972	90.003
γ, deg	90	90.317	89.962	90.051
V, Å^3	508.42	512.76	513.24	512.71
E_g^i, eV	3.26	0.27	0.43	0.20
E_{vac}, eV	—	7.32	7.19	7.48

Table 8. Vacancy in STO. Calculations with crystallographic cell (20 atoms)

Parameter	Perfect STO SG 140	STO with vacancy (8.33 %) in TiO_2	
		$S_z = 0$	$S_z = 1$
a, Å	5.488	5.538	5.568
b, Å	5.488	5.523	5.540
c, Å	7.777	7.875	7.864
α, deg	90	90.000	90.000
β, deg	90	90.000	90.000
γ, deg	90	89.029	88.429
V, Å^3	234.20	240.84	242.49
E_g^i, eV	3.39	0.44	0.71
E_{vac}, eV	—	7.56	7.43

of BTO and STO structures with oxygen vacancies and second — distribution of spins and electron charges. The electronic conductivity, as well as concentration of free carriers, increase with increasing of vacancy concentration [41]. In our calculations, concentration of oxygen vacancies is quite high. As seen in Tables 7 and 8, ionization energy for BTO structures with vacancy is 0.2–0.4 eV, for STO — 0.4–0.7 eV. In any case, defective structures are not far from conducting state. Tables 7 and 8 do not contain information about the vacancy in the TiO_2 plane with $S_z = 1$ for BTO structure (Table 7) and vacancies in the SrO plane for STO structure (Table 8) because our calculations give for these configurations conducting states.

Let us discuss now distribution of spins and electron charges in defective systems. At the beginning, we consider oxygen vacancy in the TiO_2 plane in the BTO structure (Fig. 2). Titanium atoms Ti2 and Ti4 are the nearest to the vacancy. We suppose as the initial guess that in the system with spin state $S_z = 0$, Ti2 atom has spin +1 (i. e., it has total spin "up" which is generated by spin of one unpaired electron), but Ti4 atom has spin –1 (total spin "down"). After self-consistent calculations, we find the final distribution of spins remains very close to the initial assumption: spins almost fully redistributed between these two atoms: Ti2 has spin +0.79, Ti4 has –0.79. Absolute values of spins of the other six titanium atoms do not exceed 0.1. Charge distribution correlates with distributions of spins. Thus, the Mulliken charge of Ti2 and Ti4 atoms decreases from +2.31|e| down to +2.05|e|, but charge on other Ti atoms remains almost invariable. Thus, we can conclude that spins of unpaired electrons are well localized at the nearest to the vacancy two Ti atoms whose charges decrease due to trapped electrons from a missing oxygen. Other Ti atoms hardly change their spin and charge states. Meanwhile, charges on Ba atoms remain nearly the same as in the perfect crystal, but charges of oxygen ions either decrease (to compensate for the missing oxygen atom) or remain almost the same, too. The spins of Ba and oxygen atoms are zero. Under such relaxation conditions, we get an insulating state of a system. On the other hand, the same BTO system with a vacancy in the TiO_2 plane, but with $S_z = 1$, demonstrates the conducting state. The main difference stems from the fact that in the latter case spins are not localized on two Ti atoms but redistributed almost evenly between four titanium atoms: +0.46 at Ti1 and Ti3, +0.50 at Ti2 and Ti4 (see Fig. 2; the small structural differences between systems with $S_z = 0$ and $S_z = 1$ are not essential for understanding this discussion). The charges of mentioned Ti ions decrease to +2.27|e| (Ti1, Ti3) and +2.14|e| (Ti2, Ti4). Other Ti atoms and all Ba atoms do not change their spin and charge states; oxygen atoms behave like in a system with $S_z = 0$ (see above).

Consider now the oxygen vacancy in the BaO plane in BTO (Fig. 3). The nearest Ti atoms to the vacancy, in this case, are Ti1 and Ti2, and these atoms lie on the tetragonal axis. We got insulating state for both spin states, $S_z = 0$ and $S_z = 1$. Our initial guess was that for $S_z = 0$ the nearest to the vacancy atoms Ti1 and Ti2 have spins +1 and –1, respectively. After full optimization of the system, spins remain to be localized on two atoms Ti2 (spin –0.76) and Ti8 (+0.81). Interestingly, the second from two the nearest to the vacancy atoms, Ti1, has spin only –0.17. Charges of these atoms decrease to +2.09|e| (Ti2), +2.15|e| (Ti8), and +2.20|e| (Ti1). Spins of other Ti atoms are close to zero, but their charges are almost the same as in a perfect crystal. In the case of $S_z = 1$, none of the nearest to the vacancy atoms shows visible spin. Spins are localized on Ti3 and Ti5 atoms, each of which has spin +0.86 and charge +2.15|e|. The Ti1 and Ti2 atoms have spins +0.14 and +0.05, respectively, and charges +2.22|e| and +2.23|e|, respectively. Thus, we can conclude that, in case of a vacancy in the BaO plane, the insulating state exists for both spin states ($S_z = 0$ and $S_z = 1$), spins localize on two atoms, but these atoms are not the nearest to the vacancy and they lie on the lines, which are perpendicular to the tetragonal axis. Spins of all Ba and oxygen atoms are close to zero and charges of Ba atoms are almost the same as in a perfect crystal. Charges of oxygen ions either decrease or are close to those in a perfect crystal.

Now a few words about STO structure with an oxygen vacancy. We have insulating states for both spin projections ($S_z = 0$ and $S_z = 1$) of the system with a vacancy in the TiO_2 plane and conducting states for a vacancy in the SrO plane. In general, the situation is the same, as for vacancies in the BTO. If two spins are well-localized on two Ti atoms, the system is insulating, otherwise the conducting state occurs. For example, for a vacancy in the TiO_2 plane (insulating state) with $S_z = 0$, the distribution of spins between four Ti atoms of a supercell is –0.93, +0.81, +0.14, –0.01, for $S_z = 1$ it is 0.97, 0.89, 0.08, 0.06, but for a vacancy in the SrO plane (conducting states) with $S_z = 1$ such distribution is 0.73 for two Ti atoms and 0.32 for two

other Ti atoms. At the same time, the charge on each Ti atom in all cases reduced; the situation with Sr and oxygen atoms is similar to that with Ba and oxygen atoms in BTO: spins of all Sr and oxygen atoms are close to zero, charges of Sr atoms are almost the same as in a perfect crystal, whereas charges of practically all oxygen atoms decrease.

3.2.2. The vibrational spectra of defects

Finally, we consider vibrational properties and the Raman spectra of BTO and STO with oxygen vacancies. We used the option of isotopic substitution (change of atomic masses of specific atoms) as implemented in the CRYSTAL code [43], to define the contribution of individual atoms to the vibrational mode.

A few general comments on the Raman spectra in BTO with vacancies. Raman spectra of perfect BTO crystal and that with vacancies in different planes (TiO_2 and BaO) and in various spin states are compared in Fig. 4. In all cases with vacancies, we have 114 nondegenerate TO modes (for initial 40-atoms supercell), but for a vacancy in the BaO plane with $S_z = 0$ two from these modes have an imaginary frequency. All vibrational modes in all cases are both IR- and Raman-active, therefore we will discuss only the most intensive Raman peaks in Fig. 4. In the spectra of the defective crystals, we do not see the same peaks, as in perfect crystals. Thus, all observed peaks arise due to the perturbation of the crystal lattice by the vacancies. As is seen in Fig. 4, more or less intensive peaks in the spectra of defective BTO arise in high-frequency region (> 500 cm^{-1}). These peaks are almost entirely related to vibrations of oxygen atoms. The contribution of Ba atom vibrations to the spectra is negligible. The latter vibrations can have an impact in region 50–200 cm^{-1} of spectra. Also, Ti atoms slightly contribute to the spectra in the region 200–600 cm^{-1}. Finally, vibrations of the most lightweight oxygen atoms affect the Raman spectra above ~ 500 cm^{-1}.

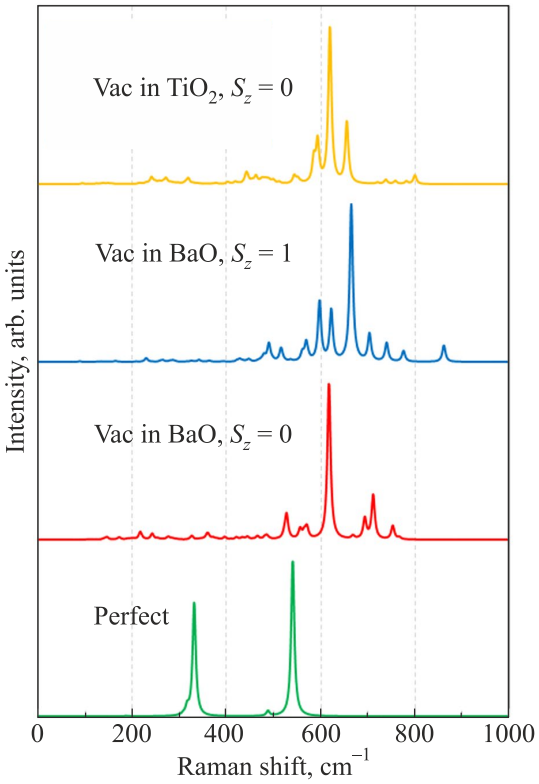

Fig. 4. The Raman spectra for BTO with vacancies in the TiO_2 and BaO planes.

The four neighboring consecutive peaks are the most intensive in the BTO spectrum with the vacancy in TiO_2 plane ($S_z = 0$): at 584 cm^{-1} (0.15), 592 cm^{-1} (0.26), 618 cm^{-1} (1.0), and 654 cm^{-1} (0.39); intensities of the Raman lines are shown in the parentheses, normalized to the line with the highest intensity. The first three peaks arise mostly from vibrations of 8 oxygen atoms nearest to the vacancy (4 equatorial and 4 axial oxygen atoms, which are connected with Ti2 and Ti4; see Fig. 2). The last peak at 654 cm^{-1} is related mainly to Ti–O stretching of four Ti atoms Ti5–Ti8 (Fig. 2) with their axial oxygen atoms and, additionally, Ti5–O stretching of the Ti5 atom and its distant equatorial oxygen atom, i. e., the nearest atoms around the vacancy do not contribute to the formation of this peak.

Let's consider now the Raman spectra for BTO with a vacancy in the BaO plane (Fig. 4). For spin state $S_z = 0$, four the most intensive peaks are seen at 526 cm^{-1} (0.16), 616 cm^{-1} (1.0), 692 cm^{-1} (0.13), and 710 cm^{-1} (0.28). In the first peak, the stretching of the Ti7 atom and its lower axial oxygen atom (Fig. 3) give the largest contribution. The maximal peak (616 cm^{-1}) is formed, mostly, by the stretching of the Ti6 atom and its left and right (on the *y* axis; Fig. 3) equatorial oxygen atoms, and the Ti4 atom with its equatorial oxygen atoms on the *x* axis. At the same time, the vibrational contribution of the nearest to the vacancy atoms to the formation of the maximal peak is negligible. Unlike the first two peaks, the vibrations of the nearest to the vacancy oxygen atoms, mainly, form peak at 692 cm^{-1}; meanwhile, the largest contributions arise from stretching of the Ti1 atom with its left (on the *y* axis) and distant (on the *x* axis) equatorial oxygen atoms. Lastly, the peak at 710 cm^{-1} also corresponds to Ti1–O stretching, but only with the lower axial oxygen atom (Fig. 3).

For the spin state $S_z = 1$ of the vacancy in the BaO plane, the picture is a little "richer", with more peaks in the spectrum; the peaks are located in the wider region of spectrum (Fig. 4). Four the most intensive peaks are observed at 596 cm^{-1} (0.38), 621 cm^{-1} (0.32), 664 cm^{-1} (1.0) and 702 cm^{-1} (0.17); the maximal peak (664 cm^{-1}) is shifted to the high-frequency spectrum region by ~ 50 cm^{-1} relatively to the maximal peak for the spin state $S_z = 0$. Vibrational analysis of corresponding modes reveals that two the most high-frequency main peaks are related mostly to the vibrations of the nearest oxygen atoms to the vacancy; at the same time, two other main peaks show quite small contribution of these atoms. For example, the main

contribution to the peak at 596 cm^{-1} is connected with the stretching of the Ti8 atom and its upper axial oxygen atom.

The Raman spectra of perfect STO crystal and that with a vacancy in the TiO_2 plane in the two different spin states are presented in Fig. 5. In both cases with vacancy, we have 54 nondegenerate TO vibrational modes (three more modes are acoustic), all are both IR- and Raman-active modes. The spectra for different spin states differ considerably; the spectrum for $S_z = 0$ reveals more peaks which are located in a wider spectral region. Six the most intensive peaks for STO with vacancy in the spin state $S_z = 0$ are: 470 cm^{-1} (0.59), 506 cm^{-1} (0.58), 532 cm^{-1} (0.37), 552 cm^{-1} (0.35), 606 cm^{-1} (0.87) and 742 cm^{-1} (1.0). For $S_z = 1$ there are five main peaks in the spectrum: 528 cm^{-1} (0.24), 597 cm^{-1} (0.15), 741 cm^{-1} (0.07), 797 cm^{-1} (1.0), 896 cm^{-1} (0.06).

We do not perform the vibrational analysis for STO as it was done above for BTO crystal, but compare here the calculated TO Raman frequencies for oxygen reduced STO with those experimentally observed at 10 K [41]. These authors reported [41] additional features in the Raman spectra of reduced STO at 505, 630, and 700 cm^{-1} with concentrations of oxygen vacancies over 10^{19} cm^{-3}, and their intensities rapidly grow with the increase of vacancy concentration. All relevant information is collected in Table 9. We present there our calculated frequencies, which are the closest to the corresponding experimental ones. The calculated frequencies are classified on the spin states, and

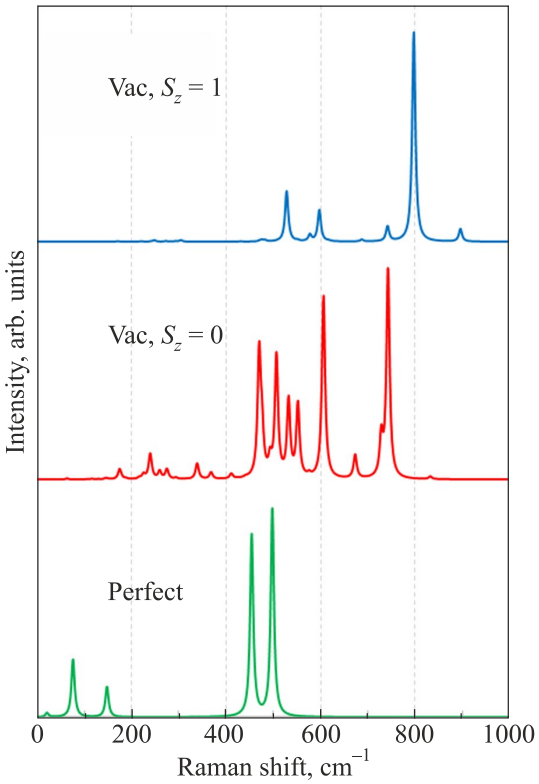

Fig. 5. The Raman spectra for STO with a vacancy in the TiO_2 plane.

Table 9. Comparison of experimentally observed at 10 K and calculated in present work TO Raman phonon frequencies (cm^{-1}) for STO with oxygen vacancies

Experiment [41]	Calculation, $S_z = 0$	Calculation, $S_z = 1$
505	493, **506**, 507	509, **528**
630	**606**, 608	**597**, 616, 620
700	673, 728, **742**	687, **741**, **797**

Note: Calculated results are for a vacancy in the TiO_2 plane.

frequencies of the most intensive peaks (see above) are given in bold. As it is seen from Table 9, the frequencies of our calculated intensive peaks are close to experimental ones.

4. Conclusions

In this study, we performed for the first time the first-principles (*ab initio*) calculations of the structural, electronic, and phonon properties of BTO and STO crystals for stoichiometric (cubic and tetragonal phases) and non-stoichiometric (with neutral oxygen vacancies in tetragonal structure) cases. The calculations for oxygen reduced crystals were performed for several spin states of a defective system. It was shown that the oxygen vacancies do not affect noticeably the macroscopic crystal structure, but change its electronic and vibrational properties. It was demonstrated that due to oxygen reduction new local vibrational modes arise at the frequencies absent in stoichiometric bulk crystals. We analyzed defect-induced phonon modes and calculated the Raman spectra for defective (with oxygen vacancies) BTO and STO crystals. The calculated well-separated and intensive new first-order Raman peaks associated with oxygen vacancies allow detecting these vacancies in experimental spectra. These new peaks arise in the high-frequency region (> 500 cm^{-1}) of the Raman spectra, outside the main Raman spectra of stoichiometric BTO and STO crystals. New spectral features arise due to vibrations of both the nearest atoms to the vacancy and more remote atoms (this may depend on the vacancy concentration). Phonon modes and shape of the Raman spectra significantly depend on the spin state of the system with oxygen vacancy but less on the location of the vacancy in different planes (TiO_2 or BaO). Our results may be useful for the analysis of experimental studies of defective STO surfaces [66].

Acknowledgments

Many thanks to R. Dovesi, R. Evarestov, N. Krainyukova, D. Gryaznov, and A. Platonenko for fruitful discussions. This study was supported by the Latvian-Ukrainian Grant LV-UA/2018/2.

1. B. Jaffe, W. R. Cook, and H. Jaffe, *Piezoelectric Ceramics*, Academic Press, London (1971).
2. M. E. Lines and A. M. Glass, *Principles and Applications of Ferroelectrics and Related Materials*, Clarendon, Oxford (1977).

3. G. A. Smolenskii, V. A. Bokov, V. A. Isupov, N. N. Krainik, R. E. Pasynkov, A. I. Sokolov, and N. K. Yushin, *Ferroelectrics and Related Materials*, Gordon and Breach, New York (1984).
4. C. R. Bowen, H. A. Kim, P. M. Weaver, and S. Dunn, *Energy Environ. Sci*. **7**, 25 (2014).
5. M. Acosta, N. Novak, V. Rojas, S. Patel, R. Vaish, J. Koruza, G. A. Rossetti, Jr., and J. Rödel, *Appl. Phys. Rev.* **4**, 041305 (2017).
6. J. Gao, D. Xue, W. Liu, C. Zhou, and X. Ren, *Actuators* **6**, 24 (2017).
7. M. M. Kuklja, E. A. Kotomin, R. Merkle, and J. Maier, *Phys. Chem. Chem. Phys*. **15**, 5443 (2013).
8. N. V. Krainyukova and V. V. Butskii, *Sur. Sci.* **454**, 628 (2000).
9. N. V. Krainyukova, V. V. Butskii, *Appl. Sur. Sci.* **235**, 43 (2004).
10. N. V. Krainyukova, V. V. Butskii, *Appl. Sur. Sci.* **235**, 32 (2004).
11. I. Z. Zhumatayeva, I. E. Kenzhina, A. L. Kozlovskiy, and M. V. Zdorovets, *J. Mater. Sci.: Mater. in Electronics* **31**(9), 6764 (2020).
12. L. Grigorjeva, D. Millers, A. I. Popov, E. A. Kotomin, and E. S. Polzik, *J. Lumin*. **72**, 672 (1997).
13. M. V. Zdorovets and A. L. Kozlovskiy, *Vacuum* **168**, 108838 (2019).
14. A. L. Kozlovskiy, I. E. Kenzhina, M. V. Zdorovets, M. Saiymova, D. I. Tishkevich, S. V. Trukhanov, and A. V. Trukhanov, *Ceramics Intern.* **45**(14), 17236 (2019).
15. M. V. Anan'ev, N. M. Bershitskaya, S. V. Plaksin, and E. Kh. Kurumchin, *Rus. J. Electrochem.* **48**(9), 879 (2012).
16. V. P. Savchyn, A. I. Popov, O. I. Aksimentyeva, H. Klym, Y. Y. Horbenko, V. Serga, A. Moskina, and I. Karbovnyk, *Fiz. Nizk. Temp*. **42**, 760 (2016) [*Low. Temp. Phys*. **42**, 597 (2016)].
17. O. I. Aksimentyeva, V. P. Savchyn, V. P. Dyakonov, S. Piechota, Y. Y. Horbenko, I. Y. Opainych, A. I. Popov, and H. Szymczak, *Mol. Cryst. Liq. Cryst*. **590**, 35 (2014).
18. L. L. Rusevich, G. Zvejnieks, A. Erba, R. Dovesi, and E. A. Kotomin, *J. Phys. Chem. A* **121**, 9409 (2017).
19. L. L. Rusevich, G. Zvejnieks, and E. A. Kotomin, *Solid State Ionics* **337**, 76 (2019).
20. C. H. Perry and D. B. Hall, *Phys. Rev. Lett*. **15**, 700 (1965).
21. P. A. Fleury, J. F. Scott, and J. M. Worlock, *Phys. Rev. Lett*. **21**, 16 (1968).
22. J. Petzelt and V. Dvorak, *J. Phys. C: Solid State Phys*. **9**, 1571 (1976).
23. J. Petzelt and V. Dvorak, *J. Phys. C: Solid State Phys*. **9**, 1587 (1976).
24. T. Nakamura, *Ferroelectrics* **137**, 65 (1992).
25. J. Petzelt, T. Ostapchuk, I. Gregora, I. Rychetský, S. Hoffmann-Eifert, A. V. Pronin, Y. Yuzyuk, B. P. Gorshunov, S. Kamba, V. Bovtun, J. Pokorný, M. Savinov, V. Porokhonskyy, D. Rafaja, P. Vaněk, A. Almeida, M. R. Chaves, A. A. Volkov, M. Dressel, and R. Waser *Phys. Rev. B* **64**, 184111 (2001).
26. P. S. Dobal and R. S. Katiyar, *J. Raman Spectrosc.* **33**, 405 (2002).
27. Yu. I. Yuzyuk, *Phys. Solid State* **54**, 1026 (2012).
28. R. A. Evarestov, E. Blokhin, D. Gryaznov, E. A. Kotomin, and J. Maier, *Phys. Rev. B* **83**, 134108 (2011).
29. R. A. Evarestov and A. V. Bandura, *J. Comput. Chem*. **33**, 1123 (2012).
30. A. Erba, Kh. E. El-Kelany, M. Ferrero, I. Baraille, and M. Rerat, *Phys. Rev. B* **88**, 035102 (2013).
31. A. Mahmoud, A. Erba, Kh. E. El-Kelany, M. Rerat, and R. Orlando, *Phys. Rev. B* **89**, 045103 (2014).
32. Yu. F. Zhukovskii, E. A. Kotomin, R. A. Evarestov, and D. E. Ellis, *Int. J. Quantum Chem*. **107**, 2956 (2007).
33. F. Gunkel, D. V. Christensen, Y. Z. Chen, and N. Pryds, *Appl. Phys. Lett*. **116**, 120505 (2020).
34. M. T. Curnan and J. R. Kitchin, *J. Phys. Chem. C* **118**, 28776 (2014).
35. J. Carrasco, F. Illas, N. Lopez, E. A. Kotomin, Yu. F. Zhukovskii, R. A. Evarestov, Yu. A. Mastrikov, S. Piskunov, and J. Maier, *Phys. Rev. B* **73**, 064106 (2006).
36. R. A. Evarestov, E. A. Kotomin, and Yu. F. Zhukovskii, *Int. J. Quantum Chem*. **106**, 2173 (2006).
37. F. El-Mellouhi, E. N. Brothers, M. J. Lucero, and G. E. Scuseria, *J. Phys.: Condens. Matter* **25**, 135501 (2013).
38. A. M. Stoneham, *Theory of Defects in Solids*, Oxford Univ. Press, Oxford (1975).
39. E. A. Kotomin and A. I. Popov, *Nucl. Instrum. Methods Phys. Res. B* **141**, 1 (1998).
40. C. J. Buchenauer, D. B. Fitchen, and J. B. Page, Jr., Chapter F-9 in: *Light Scattering Spectra of Solids*, G. B. Wright (ed.), Springer, New York (1969).
41. D. A. Tenne, I. E. Gonenli, A. Soukiassian, D. G. Schlom, S. M. Nakhmanson, K. M. Rabe, and X. X. Xi, *Phys. Rev. B* **76**, 024303 (2007).
42. R. Evarestov, E. Blokhin, D. Gryaznov, E. A. Kotomin, R. Merkle, and J. Maier, *Phys. Rev. B* **85**, 174303 (2012).
43. R. Dovesi, V. R. Saunders, C. Roetti, Orlando, C. M. Zicovich-Wilson, F. Pascale, B. Civalleri, K. Doll, N. M. Harrison, I.J. Bush, Ph. D'Arco, M. Llunel, M. Causà, Y. Noël, L. Maschìo, A. Erba, M. Rèrat, and S. Casassa, *CRYSTAL17 User's Manual*, University of Torino, Torino (2017).
44. S. Piskunov, E. Heifets, R.I. Eglitis, and G. Borstel, *Comput. Mater. Sci*. **29**, 165 (2004).
45. T. Bredow, K. Jug, and R. A. Evarestov, *Phys. Status Solidi B* **243**, R10 (2006).
46. L. L. Rusevich, G. Zvejnieks, E. A. Kotomin, M. Maček Kržmanc, A. Meden, Š. Kunej, and I. D. Vlaicu, *J. Phys. Chem. C* **123**, 2031 (2019).
47. D. I. Bilc, R. Orlando, R. Shaltaf, G. M. Rignanese, J. Iniguez, and Ph. Ghosez, *Phys. Rev. B* **77**, 165107 (2008).
48. G. Zvejnieks, L. L. Rusevich, D. Gryaznov, and E. A. Kotomin, *Phys. Chem. Chem. Phys*. **21**, 23541 (2019).
49. G. J. B. Hurst, M. Dupuis, and E. Clementi, *J. Chem. Phys*. **89**, 385 (1988).

50. B. Kirtman, F. L. Gu, and D. M. Bishop, *J. Chem. Phys.* **113**, 1294 (2000).
51. R. Dovesi, B. Kirtman, L. Maschio, J. Maul, F. Pascale, and M. Rérat, *J. Phys. Chem. C* **123**, 8336 (2019).
52. L. Maschio, B. Kirtman, M. Rérat, R. Orlando, and R. Dovesi, *J. Chem. Phys.* **139**, 164101 (2013).
53. L. Maschio, B. Kirtman, M. Rérat, R. Orlando, and R. Dovesi, *J. Chem. Phys*. **139**, 164102 (2013).
54. *Ternary Compounds, Organic Semiconductors*, in: O. Madelung, U. Rössler, M. Schulz (eds.), Landolt-Börnstein — Group III Condensed Matter, vol. 41E, Springer, Berlin (2000).
55. L. Cao, E. Sozontov, and J. Zegenhagen, *Phys. Status Solidi A* **181**, 387 (2000).
56. S. H. Wemple, *Phys. Rev. B* **2**, 2679 (1970).
57. K. van Benthem, C. Elsässer, and R. H. French, *J. Appl. Phys.* **90**, 6156 (2001).
58. W. Zhong, R. D. King-Smith, and D. Vanderbilt, *Phys. Rev. Lett*. **72**, 3618 (1994).
59. W. G. Spitzer, R. C. Miller, D. A. Kleinman, and L. E. Howarth, *Phys. Rev.* **126**, 1710 (1962).
60. M. Adachi, Y. Akishige, T. Asahi, K. Deguchi, K. Gesi, K. Hasebe, T. Hikita, T. Ikeda, Y. Iwata, M. Komukae, T. Mitsui, E. Nakamura, N. Nakatani, M. Okuyama, T. Osaka, A. Sakai, E. Sawaguchi, Y. Shiozaki, T. Takenaka, K. Toyoda, T. Tsukamoto, and T. Yagi, in *Landolt–Börnstein — Group III Condensed Matter*, Y. Shiozaki, E. Nakamura and T. Mitsui (eds.), Springer-Verlag, Berlin, Heidelberg (2001), vol. 36A1.
61. P. Hermet, M. Veithen, and Ph. Ghosez, *J. Phys.: Condens. Matter* **21**, 215901 (2009).
62. U. D. Venkateswaran, V. M. Naik, and R. Naik, *Phys. Rev. B* **58**, 14256 (1998).
63. H. Unoki and T. Sakudo, *J. Phys. Soc. Jpn*. **23**, 546 (1967).
64. D. Gryaznov, E. Blokhin, A. Sorokine, E. A. Kotomin, R. A. Evarestov, A. Bussmann-Holder, and J. Maier, *J. Phys. Chem. C* **117**, 13776 (2013).
65. A. Stashans and F. Vargas, *Mater. Lett*. **50**, 145 (2001).
66. N. V. Krainyukova, V. O. Hamalii, A. V. Peschanskii, A. I. Popov, and E. A. Kotomin, *Fiz. Nizk. Temp*. **46**, 877 (2020) [*Low Temp. Phys*. **46**, 740 (2020)].

Ab initio розрахунки структурних, електронних та коливальних властивостей кристалів перовскитів $BaTiO_3$ та $SrTiO_3$ з кисневими вакансіями

L. L. Rusevich, E. A. Kotomin, G. Zvejnieks, A. I. Popov

Виконано розрахунки з перших принципів (*ab initio*) структурних, електронних і фононних властивостей кубічних та низькотемпературних тетрагональних фаз кристалів перовскитів $BaTiO_3$ і $SrTiO_3$ як стехіометричних, так і нестехіометричних (з нейтральними кисневими вакансіями). Для розрахунків використано комп'ютерний код CRYSTAL17 у наближенні лінійної комбінації атомних орбіталей із застосуванням розширеного гібридного обмінно-кореляційного функціонала B1WC з теорії функціонала щільності (DFT), а також підходу з використанням періодичної суперкомірки. Розглянуто різні можливі спінові стани дефектної системи за допомогою необмежених (з відкритою оболонкою) DFT-розрахунків. Показано, що зменшення кисню призводить до появи нових локальних коливальних мод, пов'язаних з кисневими вакансіями, а також нових піків першого порядку в спектрах комбінаційного розсіювання світла, які можуть бути використані для ідентифікації дефектів. Розраховані спектри комбінаційного розсіювання світла для різних положень вакансій і спінів системи, а також інші властивості дефектних кристалів порівнюються з відповідними експериментальними даними.

Ключові слова: $BaTiO_3$, $SrTiO_3$, киснева вакансія, гібридні обчислення DFT, інфрачервоні спектри, спектри комбінаційного розсіювання світла.